processes

Article

Erosion Behavior and Prediction Model of Intelligent Filling Tools Under Flow-Path Switching Conditions

Kai Zuo [1,2], Binggang Wang [1,2], Yunchi Zhang [1,2], Chuangang Liu [1,2], Jingchao Liu [1,2] and Mingxuan Zhang [3,*]

[1] CNOOC Energy Technology & Services Limited Key Laboratory for Offshore Completion, Tianjin 300452, China; zuokai@cnooc.com.cn (K.Z.); wangbg3@cnooc.com.cn (B.W.); zhangych43@cnooc.com.cn (Y.Z.); liuchg@cnooc.com.cn (C.L.); liujch4@cnooc.com.cn (J.L.)
[2] CNOOC EnerTech-Drilling & Production Co., Tianjin 300452, China
[3] College of Petroleum Engineering, China University of Petroleum, Beijing 102249, China
* Correspondence: 2024211026@student.cup.edu.cn

Abstract

Flow-path switching is a key operating condition that enables flow regulation, zonal conversion, and filling-path redirection in sand-control completions. The associated flow characteristics directly govern the operational stability and service reliability of intelligent filling tools. Most existing studies have addressed erosion only under simple geometries such as pipe contractions and expansions, leaving the dominant erosion-controlling factors and rapid erosion-rate prediction methods for sand-control filling tools under flow-path switching conditions insufficiently understood. This study developed a Fluent-based numerical model of solid–liquid two-phase erosion for intelligent filling tools and characterizes the wall-erosion distribution pattern during flow-path switching. Guided by field practice, multi-factor simulations were performed over the reduction angle, cutting particle size, inlet flow capacity, flow-switching direction, opening area, and structural form. On this basis, a maximum-erosion-rate prediction model was constructed using a logarithmic transformation combined with a stepwise quadratic response-surface method. This regression-based approach was deliberately chosen over machine-learning black-box models, whose limited interpretability and small-sample reliability make it difficult to reveal the underlying physical mechanisms; in contrast, the proposed model yields an explicit algebraic expression whose significant interaction and quadratic terms directly reflect the coupling between structural and operating parameters, while the logarithmic transformation accommodates erosion-rate fluctuations spanning several orders of magnitude. The results show that the factors rank in influence as follows: flow-switching direction > opening area > reduction angle > inlet flow capacity > cutting particle size > structural form. The established prediction model attained a coefficient of determination of about 0.951 and an adjusted coefficient of determination of about 0.901; combined with the significance test and a residual analysis, the model can effectively characterize the coupling influence of structural parameters and operating parameters on the erosion rate. These findings provide quantitative guidance for the erosion-resistant structural design, field operating-parameter selection, and preliminary service-life assessment of intelligent filling tools in offshore sand-control well-completion operations. The prediction model is further validated through jetting-erosion bench tests; the measured erosion rates agree closely with the model-predicted values, confirming the practical reliability of the model and its capability to serve as an engineering reference for the erosion-resistant design and service-life assessment of intelligent filling tools in sand-control well-completion operations.

Academic Editor: Qingbang Meng

Received: 4 June 2026
Revised: 4 July 2026
Accepted: 22 July 2026
Published: 6 August 2026

Keywords: flow-path switching; intelligent sand-control filling tool; solid–liquid two-phase erosion; maximum erosion-rate prediction; logarithmic stepwise response surface regression; orthogonal experimental design

1. Introduction

As the development of complex sandstone oil and gas reservoirs continues to advance toward zonal control, refined sand management, and intelligent operations, conventional gravel-packing sand-control techniques have become increasingly unable to fully meet field requirements in terms of flow-path regulation, interval conversion, and adaptability to complex operating conditions. Intelligent filling tools can achieve the dynamic control of zonal sand-control operations through flow-path switching, an opening adjustment, and filling-path redirection, thereby improving the flexibility and reliability of sand-control operations. However, during the flow-path switching process, the sand-laden fluid undergoes complex flow behaviors, including local contraction, abrupt changes in flow direction, an increased flow velocity, and high-velocity particle impingement. These phenomena can readily induce localized and concentrated erosion on the inner wall of the tool, particularly in the reduction section, around the edges of openings, and in flow-turning regions. The continued progression of erosion damage may alter the internal flow-path geometry of the tool, affect the accuracy of the flow distribution and filling stability, and, in severe cases, reduce the service reliability of the tool. Therefore, investigating the particle erosion behavior and corresponding prediction methods of intelligent filling tools under flow-path switching conditions is of great engineering significance for structural optimization, field operating-parameter control, and service-life evaluation.

Solid-particle erosion has long been an important concern in oil and gas engineering, chemical pipelines, fluid machinery, and related fields. Early studies mainly focused on the mechanisms of particle impact, material removal, and wall-surface damage. Finnie explained the erosion process from the perspective of particle cutting, indicating that the particle impact angle and impact velocity have significant effects on material removal. Levy, Bitter, Neilson, Gilchrist, and others further analyzed the mechanisms of solid-particle erosion in terms of plastic deformation, crack initiation, material spalling, and secondary impact [1–6]. With the development of computational fluid dynamics and the discrete phase model, the CFD-DPM approach has been widely used to track particle trajectories, analyze particle–wall collision processes, and predict wall erosion distributions [7–12]. On this basis, Oka, Zhang, Arabnejad, and others proposed various empirical and mechanistic erosion models that correlate the erosion rate with factors such as the particle velocity, impact angle, particle size, particle mass flow rate, and wall material properties, thereby providing an important methodological foundation for erosion predictions in complex flow-path structures [13–17].

In the oil and gas industry, particle erosion in components such as choke valves, control valves, elbows, tees, contraction pipes, reducers, and sand screens has been extensively investigated. Existing studies have shown that elbows and tees are prone to the formation of high-erosion regions on the outer bend wall, at the blind end, or within local recirculation zones because of significant changes in the flow direction and inertial particle migration. In contrast, choke valves, control valves, and contraction structures tend to induce concentrated particle impingement and rapid wall degradation owing to local throttling, abrupt increases in the flow velocity, and high-speed jetting effects [18–28]. In addition, erosion, plugging, and structural failure in sand-control screens, pre-packed screens, and downhole filtration media are considered critical factors affecting the longterm stability of sand-control completions [29–33]. Although the aforementioned structures are not entirely identical to the intelligent filling tool in terms of function and geometry, they share several common characteristics, including local contraction, abrupt changes in flow direction, enhanced velocity gradients, and high-velocity particle impingement. Therefore, they can provide theoretical support and methodological guidance for the erosion analysis of the flow-channel switching tool investigated in this study.

However, significant differences still exist between previous studies and the research object of this study. Most existing investigations have focused primarily on conventional pipe fittings, valve structures, or screen structures, in which the flow paths are relatively fixed. These studies usually emphasize the influence of a single structural parameter or a limited number of operating parameters on erosion. In contrast, the internal flow within the intelligent filling tool under flow-channel switching conditions is more complex. Its erosion behavior is governed not only by the particle size and inlet flow rate, but also by the coupled effects of multiple factors, including the contraction angle, flow-channel switching direction, opening area, and structural configuration.

In particular, in regions involving flow-channel convergence, opening redirection, and local contraction, the particle trajectories, impact angles, local velocity fields, and wall erosion locations may vary significantly with changes in the flow direction and structural parameters, resulting in variations in the maximum erosion rate across several orders of magnitude. Therefore, existing studies still pay insufficient attention to the multi-factor coupled erosion behavior in practical intelligent filling tools. Moreover, the quantitative ranking of the relative importance of different factors remains unclear, and a rapid erosion prediction method that combines a high predictive accuracy with physical interpretability is still lacking. Through orthogonal experimental design and a range analysis, the influence degree and importance ranking of each factor on the maximum erosion rate were determined. Furthermore, considering the order-of-magnitude variation in the erosion rate and its nonlinear response characteristics, a stepwise quadratic response surface prediction model based on a logarithmic transformation was established to improve the fitting capability and physical interpretability of the model [34–37]. Meanwhile, jet erosion experiments were conducted to validate the numerical simulation and prediction results. The findings of this study can provide a theoretical basis and engineering reference for erosion-resistant structural design, field operating-parameter optimization, and the preliminary service-life evaluation of intelligent filling tools.

In addition, recent research on the structural response and optimization of engineering structures under complex service conditions [38] provides a useful reference for extending the present work: the coupled numerical-simulation and regression-based prediction framework developed here can, in future research, be combined with conservation of mass equation and scale-up studies to generalize the erosion-resistant design of solid-particle-laden flow structures.

2. Theoretical Model and Numerical Method

Under flow-path switching conditions, the internal flow field of the novel intelligent filling structure is characterized by local contraction, abrupt changes in the flow direction, and high-velocity jetting. When the sand-laden fluid passes through the switching flow path, it is prone to forming a non-uniform velocity field and pressure gradient, thereby altering particle trajectories and their impact behavior on the wall surfaces. To analyze the erosion characteristics under this operating condition, a numerical erosion model for solid–liquid two-phase flow was established in this study. The continuous phase was solved using the Eulerian approach, while the particle phase was tracked using the discrete phase method. In addition, a wall erosion model was incorporated to calculate the erosion rate. The continuous-phase fluid satisfies the following mass and momentum conservation equations:

(1) Mass conservation equation:

$$\frac{\partial \rho}{\partial t} + \frac{\partial \rho u}{\partial x} + \frac{\partial \rho v}{\partial y} + \frac{\partial \rho w}{\partial z} = 0 \tag{1}$$

where t is time, s; ρ is the fluid density, kg/m^3; and u, v, and w are the fluid velocity components in the x, y, and z directions, respectively.

(2) Momentum conservation equation:

$$\begin{aligned} \frac{\partial(\rho u)}{\partial t} + \nabla \cdot (\rho u U) = -\frac{\partial P}{\partial x} + \frac{\partial \tau_{xx}}{\partial x} + \frac{\partial \tau_{yx}}{\partial y} + \frac{\partial \tau_{zx}}{\partial z} + \rho f_x \\ \frac{\partial(\rho v)}{\partial t} + \nabla \cdot (\rho v U) = -\frac{\partial P}{\partial y} + \frac{\partial \tau_{xy}}{\partial x} + \frac{\partial \tau_{yy}}{\partial y} + \frac{\partial \tau_{zy}}{\partial z} + \rho f_y \\ \frac{\partial(\rho w)}{\partial t} + \nabla \cdot (\rho w U) = -\frac{\partial P}{\partial z} + \frac{\partial \tau_{xz}}{\partial x} + \frac{\partial \tau_{yz}}{\partial y} + \frac{\partial \tau_{zz}}{\partial z} + \rho f_z \end{aligned} \tag{2}$$

where P is the pressure, Pa; τ is the component of the viscous stress tensor, Pa; μ is the dynamic viscosity of the liquid, Pa·s; and F_x, F_y, and F_z are the body forces per unit mass in the x, y, and z directions, respectively, m/s^2.

Considering the occurrence of flow separation, strong shear, and local acceleration in the flow-path switching region, the realizable k–ε turbulence model [10] was adopted in this study to describe the turbulent flow of the continuous phase. This model shows a good applicability to complex shear flows and separated flows, and can be used to obtain the velocity-field and pressure-field distributions within the switching flow path.

The particle phase was solved using the discrete phase model. Because the sand particle volume fraction in the sand-laden fluid considered in this study was relatively low, inter-particle collisions were neglected in the calculation. The analysis mainly focused on particle motion under the effects of fluid drag and other additional forces. The governing equation for particle motion is expressed as follows:

$$\frac{du_{\mathrm{p}}}{dt} = \frac{F_{\mathrm{D}}}{\rho_{\mathrm{p}}} + \mathrm{g} + \sum F_{\mathrm{other}} \tag{3}$$

where u_p is the particle velocity, m/s; ρ_p is the particle density, kg/m^3; and F_D is the fluid drag force, N, which is commonly calculated using the Schiller–Naumann model.

After particles collide with the wall, their rebound behavior directly affects their subsequent trajectories and secondary impact locations. To characterize the kinetic-energy dissipation and directional change during particle–wall collisions, normal and tangential restitution coefficients were employed in this study to describe the particle–wall collision characteristics, as expressed as follows:

$$\varepsilon_N = 0.993 - 1.76\theta + 1.56\theta^2 - 0.49\theta^3 \tag{4}$$

$$\varepsilon_T = 0.988 - 1.66\theta + 2.11\theta^2 - 0.67\theta^3 \tag{5}$$

where e and e_{t} are the normal and tangential restitution coefficients of the particle, respectively.

Wall erosion wear was calculated using the generic erosion model. In this model, the erosion rate is expressed as a comprehensive function of the particle mass flow rate, particle-size function, impact-angle function, particle impact velocity, and wall surface area.

It can therefore effectively characterize the localized wall erosion caused by sand-laden flow in complex flow passages. The erosion-rate expression is given as follows:

$$R_{erosion} = \sum \frac{m_p(d_p)f(\alpha)v^{b(v)}}{A_{face}} \tag{6}$$

where m_p is the particle mass flow rate; $C(d_p)$ is the particle-size function; f(a) is the impact-angle function; v_p is the particle impact velocity; $b(v_p)$ is the velocity exponent function; and A_{face} is the wall surface area.

In summary, a numerical erosion calculation method applicable to flow-path switching conditions in novel intelligent filling tools was established in this study based on the governing equations of the continuous phase, the realizable *k*–*ε* turbulence model, the discrete-phase particle motion model, the particle–wall collision model, and the generic erosion model. This method can simultaneously obtain the internal velocity field, pressure field, particle trajectories, and maximum wall erosion rate of the tool, thereby providing a theoretical basis for the subsequent analysis of the effects of parameters such as the reduction angle, particle size, inlet flow capacity, and inlet pressure on the erosion characteristics.

3. Numerical Simulation of Flow-Path Switching

Establishment of the Finite Element Model and Boundary Condition Settings

The inlet area of Model 1 was 7853.98 mm^2, the outlet area was 4586.28 mm^2, and the total length was 527.47 mm. The inlet area of Model 2 was 2827.43 mm^2, the outlet area was 4586.28 mm^2, and the total length was 527.47 mm. Owing to the geometric complexity of the models, each model was divided into three parts for meshing. Local mesh refinement was applied to the middle transition section, and boundary-layer meshes were added with five layers. The geometric models are shown in Figure 1, and the corresponding mesh, including the five-layer boundary-layer (inflation) mesh applied at the walls to resolve the near-wall region, is shown in Figure 2.

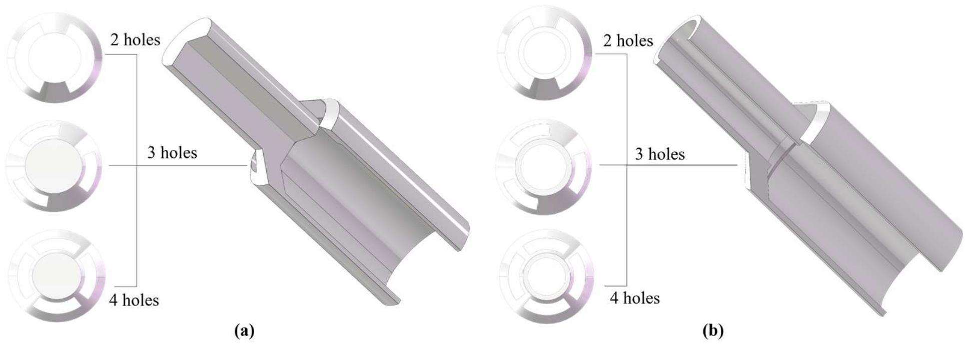

Figure 1. Geometric models of the intelligent filling tool: (**a**) Model 1; (**b**) Model 2.

For the mesh-independence analysis, the maximum erosion wear rate under the flow-path switching condition was selected as the evaluation criterion. The results became relatively stable when the mesh numbers were approximately 80,000, 150,000, and 230,000. When the mesh was refined from 150,000 to 230,000 cells, the change in the maximum erosion rate was below 5% and the erosion hot spot remained at the reduction shoulder and the opening edges. Considering the numerical accuracy and stability, the mesh with approximately 230,000 cells was ultimately adopted for the subsequent calculations, as summarized in Table 1.

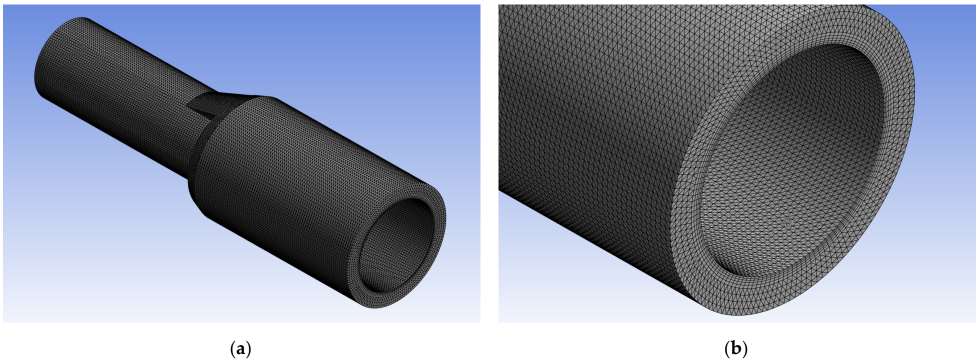

Figure 2. Mesh generation of the intelligent filling tool: (**a**) overall mesh of the model; (**b**) five-layer boundary-layer (inflation) mesh.

Table 1. Grid-independence verification of the maximum erosion rate.

Mesh Scheme	Number of Cells	Deviation of the Maximum Erosion Rate from the 230,000-Cell Mesh (%)	Location of Maximum Erosion
Coarse	≈80,000	<5	Reduction shoulder/opening edge
Medium	≈150,000	<5	Reduction shoulder/opening edge
Fine (adopted)	≈230,000	\	Reduction shoulder/opening edge

In this study, the simulated operating parameters were designed according to the actual field operating conditions. The geometric models of the flow-path switching tool (Model 1 and Model 2) were reconstructed in a one-to-one correspondence with the actual downhole intelligent filling tool used in the target offshore sand-control wells, so that the reduction section, the opening structure, and the flow-switching passage reproduced the real tool geometry rather than a simplified analogue. Likewise, the ranges of the controlling factors were not chosen arbitrarily, but were bounded by field-measured data: the cutting particle size (3–5 mm) corresponded to the size distribution of the formation sand and gravel-pack particles produced on site, the inlet flow capacity matched the range of pump displacement applied during field filling operations, and the fluid medium and sand concentration were set to the field-representative values for the water-based carrier fluid. Consequently, the simulation conditions were field-consistent in both the geometry and operating regime, which ensured that the resulting erosion law and prediction model were directly transferable to the engineering site. The required boundary conditions are listed in Table 2. The key settings used in all simulations are as follows: a fluid density of 1000 kg/m^3 (water), a dynamic viscosity of 1.0×10^{-3} Pa·s, a sand particle density of 2650 kg/m^3, a DPM mass flow rate of 0.01 kg/s per injection surface, a normal restitution coefficient of 0.8, a tangential restitution coefficient of 0.9, a wall material hardness set to that of carbon steel (Vickers hardness: 120 HV), a convergence criterion of 10^{-5} for all residuals, and steady-state initialization with 500 DPM iterations after the continuous-phase solution reached convergence. These settings are summarized in Table 2.

Table 2. Key numerical settings and boundary conditions used in the simulations.

Item	Value/Setting
Continuous-phase turbulence model	Realizable k-ε model
Particle-phase model	Discrete phase model (DPM)
Wall-erosion model	Generic erosion model
Carrier-fluid density	1000 kg/m^3 (water)
Dynamic viscosity	1.0×10^{-3} Pa·s
Sand-particle density	2650 kg/m^3
DPM mass flow rate	0.01 kg/s per injection surface
Normal restitution coefficient	0.8

Table 2. *Cont.*

Item	Value/Setting
Tangential restitution coefficient	0.9
Wall material/hardness	Carbon steel, 120 HV (Vickers)
Convergence criterion (all residuals)	10^{-5}
Solution strategy	Steady state; 500 DPM iterations after continuous-phase convergence

4. Analysis of Erosion Characteristics Under Flow-Path Switching Conditions

4.1. Erosion Sensitivity Analysis and Erosion Distribution Characteristics

A single-factor analysis can only evaluate the influence of one factor on the response, and cannot determine the relative significance of different factors. Therefore, an orthogonal experimental design was adopted to identify the significance of each influencing factor. In this study, the erosion rate was selected as the evaluation index. Based on the factors affecting the erosion rate, an orthogonal experiment involving six factors and multiple levels was designed, as shown in Table 3.

Table 3. Orthogonal design table for flow-path switching.

Case	Reduction Angle	Cutting Particle Size (mm)	Inlet Flow Rate (m^3/min)	Flow-Switching Direction	Opening Area	Model 1 Model 2	Erosion Rate (kg/(m^2·s))
1	20°	3	1	Forward	2 holes	1	4.17281×10^{-8}
2	20°	4	1.5	Reverse	4 holes	1	1.28494×10^{-6}
3	20°	5	2	Forward	3 holes	1	2.99801×10^{-6}
4	20°	4	1.5	Forward	4 holes	1	5.59197×10^{-7}
5	45°	3	1.5	Forward	4 holes	1	1.67798×10^{-6}
6	45°	4	1	Forward	3 holes	1	5.86103×10^{-6}
7	45°	5	1.5	Forward	4 holes	1	1.41630×10^{-6}
8	45°	4	2	Reverse	2 holes	1	8.67874×10^{-5}
9	90°	3	2	Forward	4 holes	1	2.70374×10^{-6}
10	90°	4	1.5	Forward	2 holes	1	3.85047×10^{-5}
11	90°	5	1	Reverse	4 holes	1	1.26029×10^{-5}
12	90°	4	1.5	Forward	3 holes	1	1.28691×10^{-5}
13	45°	3	1.5	Reverse	3 holes	1	2.23369×10^{-5}
14	45°	4	2	Forward	4 holes	1	4.34132×10^{-6}
15	45°	5	1.5	Forward	2 holes	1	7.01541×10^{-5}
16	45°	4	1	Forward	4 holes	1	3.54831×10^{-5}
17	20°	3	1	Forward	2 holes	2	1.25652×10^{-6}
18	20°	4	1.5	Reverse	4 holes	2	6.47857×10^{-6}
19	20°	5	2	Forward	3 holes	2	3.28570×10^{-6}
20	20°	4	1.5	Forward	4 holes	2	7.57457×10^{-6}
21	45°	3	1.5	Forward	4 holes	2	1.98972×10^{-6}
22	45°	4	1	Forward	3 holes	2	1.42173×10^{-6}
23	45°	5	1.5	Forward	4 holes	2	1.85266×10^{-6}
24	45°	4	2	Reverse	2 holes	2	7.41756×10^{-6}
25	90°	3	2	Forward	4 holes	2	3.67086×10^{-6}
26	90°	4	1.5	Forward	2 holes	2	1.66896×10^{-6}
27	90°	5	1	Reverse	4 holes	2	7.58061×10^{-5}
28	90°	4	1.5	Forward	3 holes	2	4.42009×10^{-5}
29	45°	3	1.5	Reverse	3 holes	2	7.54309×10^{-5}
30	45°	4	2	Forward	4 holes	2	4.95810×10^{-6}
31	45°	5	1.5	Forward	2 holes	2	2.11538×10^{-6}
32	45°	4	1	Forward	4 holes	2	1.86351×10^{-6}

Six factors were selected as the research variables, namely the reduction angle, cutting particle size, inlet flow capacity, flow-switching direction, opening area, and structural form. The orthogonal experiments were carried out according to the orthogonal array. The experimental scheme and corresponding results are presented in Table 3.

https://doi.org/10.3390/pr14152523

Based on the single-factor simulations, the flow-field feature extraction, and the subsequent range analysis of the orthogonal experimental results, the effects of the key factors on the erosion rate of the intelligent filling tool under flow-path switching conditions are summarized as follows:

1. Effect of Flow-Switching Direction on Erosion Rate

The flow-switching direction is the primary factor responsible for severe fluctuations in the erosion rate. The range analysis showed that the average erosion rate under reverse flow is significantly higher than that under forward flow. In forward flow, the fluid passes smoothly through the reduction section. In contrast, under reverse flow, the direction of the sand-laden fluid conflicts abruptly with the internal contraction cavity of the tool. Owing to their strong inertia, the particles cannot promptly follow the turning flow field, and therefore directly impinge on the internal shoulder and wall surfaces with a relatively high kinetic energy. This mismatch between the flow direction and the structural geometry leads to a pronounced local concentration of kinetic energy, which is the main reason for the sharp increase in the erosion risk under reverse-flow conditions.

2. Effect of Cutting Particle Size on Erosion Rate

The influence of the particle size on the erosion rate exhibited a typical trade-off between the particle mass and the flow-following capability. Within the parameter range considered in this study, particles with a diameter of approximately 3 mm showed a relatively high erosion risk. This is because particles of this size possess sufficient mass and kinetic energy while also maintaining good flow-following capability, enabling them to follow complex streamlines and accurately impinge on erosion-sensitive wall surfaces at flow-path turning locations. In contrast, very small particles are dominated by fluid drag and are less likely to strike the wall, whereas very large particles, such as 5 mm particles, have a higher kinetic energy, but excessive inertia. As a result, they tend to undergo noncritical collisions or settling before entering the core contraction region, leading to a slower increase in the maximum erosion rate (Figures 3 and 4).

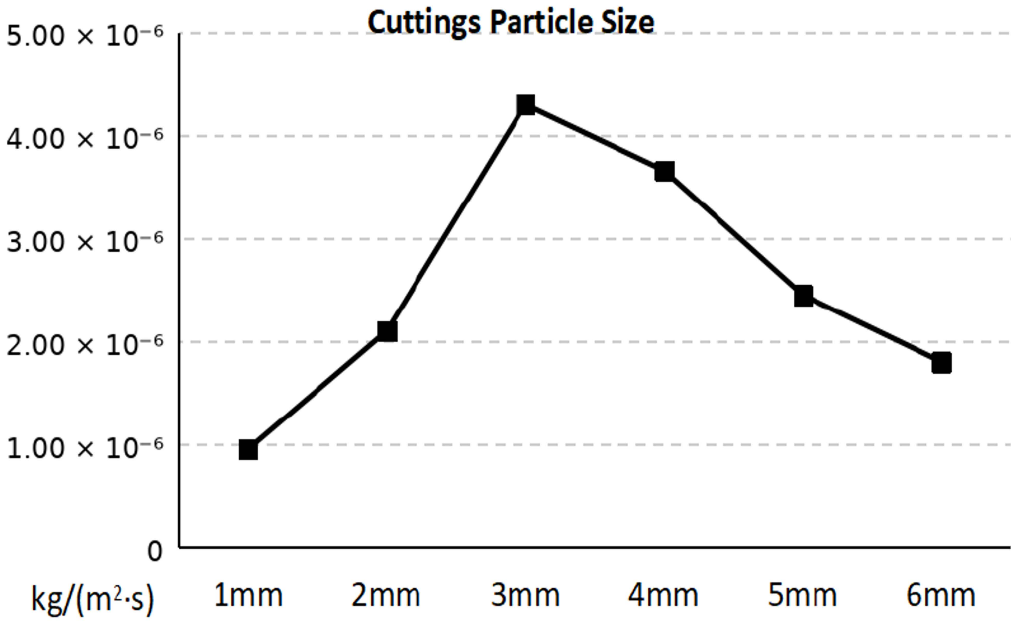

Figure 3. Effect of cutting particle size on the maximum erosion rate.

Figure 4. Erosion-rate distribution under different cutting particle sizes.

3. Effect of Reduction Angle on Erosion Rate

The reduction angle directly determines the velocity gradient in the flow-path contraction region. The simulation results showed that a small reduction angle of 20° provides the most favorable flow-guiding effect, with smooth internal streamlines and a relatively low particle collision frequency. When the reduction angle increases to 45° and 90°, the abrupt change in the flow-path cross section induces strong flow separation and recirculation zones, thereby increasing the probability of repeated particle impacts on local wall surfaces. Although the erosion rate may decrease slightly at the 90° reduction angle owing to the vortex-shielding effect, reducing the reduction angle is, in general, an effective approach for mitigating damage in the guiding section (Figures 5 and 6).

Figure 5. Effect of reduction angle on the maximum erosion rate.

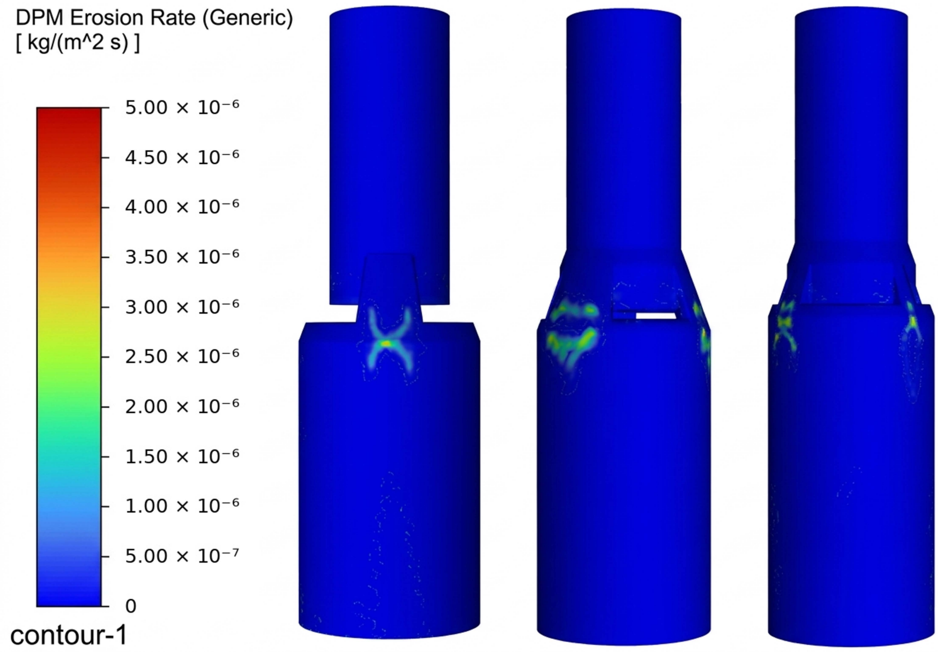

Figure 6. Erosion-rate distribution under different reduction angles.

4. Effects of Inlet Flow Rate and Structure on Erosion Rate

The inlet flow capacity showed a positive correlation with the erosion rate. An increase in the flow rate directly enhances the initial impact momentum of particles. However, in complex flow passages, the influence of flow rate is often modulated by the flow direction and the reduction angle. The effect of the structural form, namely a solid or hollow structure, is mainly reflected by the variation in the internal cavity volume. The hollow structure, owing to its larger buffering space, facilitates the early dissipation of fluid kinetic energy under certain operating conditions, and thus exhibits slightly better erosion-resistance reliability than the solid structure (Figures 7 and 8).

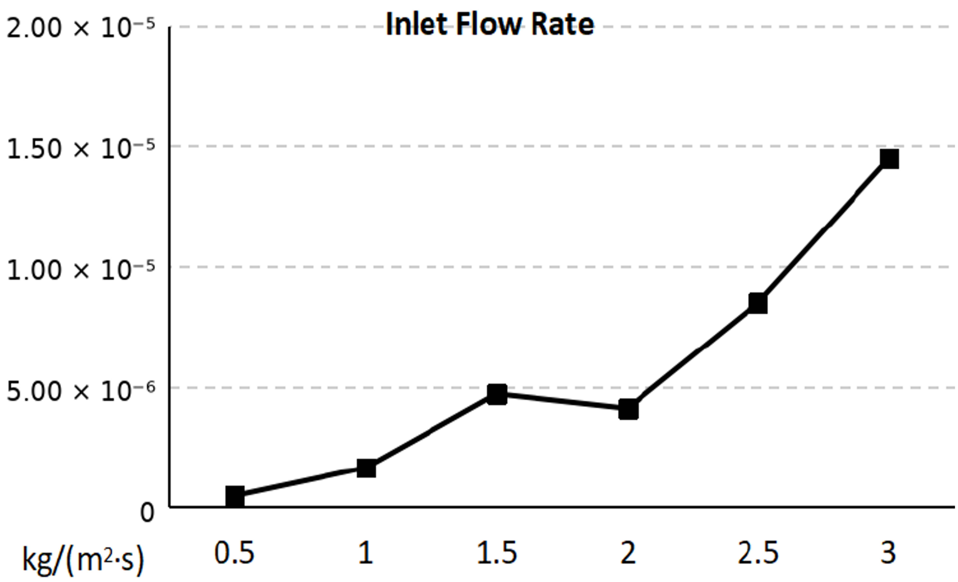

Figure 7. Effect of inlet flow capacity on the maximum erosion rate.

Figure 8. Erosion-rate distribution under different inlet flow capacities.

5. Effect of Opening Area on Erosion Rate

The opening area has a significant influence on the erosion rate; however, its effect is not simply monotonic. Within the range of operating conditions considered in this study, the four-opening structure exhibited the lowest average erosion rate, whereas the three-opening structure showed the highest average erosion rate. This indicates that a coupling effect may exist among the opening area, flow-switching direction, and local flow-path configuration. Increasing the opening area can help reduce the local jet velocity; however, if the hole arrangement causes particles to impinge in a concentrated manner, localized high-erosion regions may still form (Figures 9 and 10).

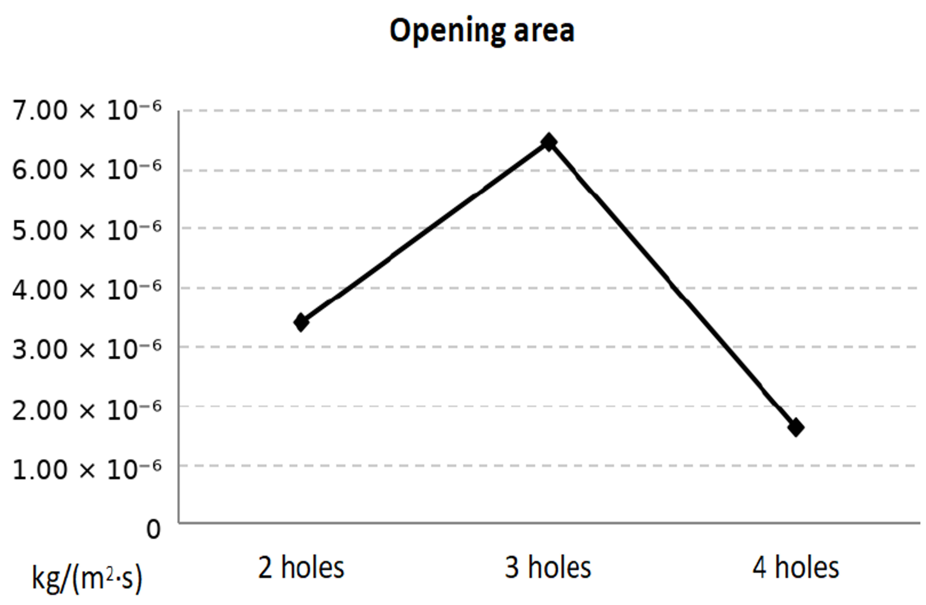

Figure 9. Effect of opening area on the maximum erosion rate.

In summary, to reduce erosion damage to the intelligent filling tool under flow-path switching conditions, a forward flow, a small reduction angle of 20°, and a multi-opening structure should be preferentially adopted in both structural design and field operation, together with reasonable inlet flow capacity control.

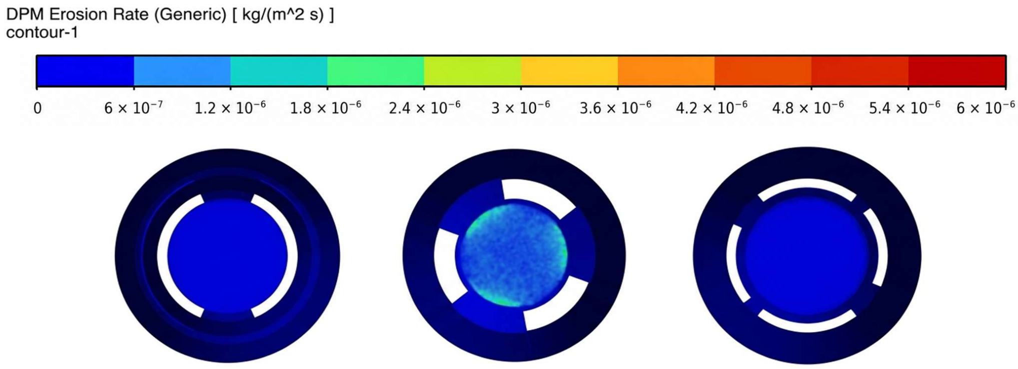

Figure 10. Erosion-rate distribution under different opening areas.

4.2. Sensitivity Analysis

1. Range Analysis

Based on the 32 sets of numerical simulation results in Table 3, a range analysis was conducted for factors that included the reduction angle, cutting particle size, inlet flow capacity, flow-switching direction, opening area, and structural form. Because the occurrence frequency of each factor level was not completely consistent, the average value of the maximum erosion rate at each level was used for the statistical analysis in this study. Specifically, the 32-run design was generated from an L32 orthogonal array; for binary factors (flow-switching direction, structural form), each level appears in exactly 16 runs, whereas for the three-level factors (reduction angle, particle size, inlet flow capacity, opening area), the level counts are unequal across the combined array. The use of the level-average erosion rate—rather than the sum—corrects for this imbalance and ensures that the range R is a consistent measure of factor importance, regardless of the number of replicates per level (Table 4).

Table 4. Range analysis table.

Factors	Lowest Erosion-Rate Level	Minimum Mean Value	Highest Erosion-Rate Level	Maximum Mean Value	Range R	Influence Ranking
Flow-switching direction	Forward flow	1.944×10^{-6}	Reverse	6.545×10^{-6}	4.602×10^{-6}	1
Opening area	4 holes	1.869×10^{-6}	3 holes	6.369×10^{-6}	4.501×10^{-6}	2
Reduction angle	20°	1.526×10^{-6}	90°	4.011×10^{-6}	2.484×10^{-6}	3
Inlet flow rate	1	1.618×10^{-6}	1.5	3.976×10^{-6}	2.359×10^{-6}	4
Cutting particle size	5 mm	2.021×10^{-6}	3 mm	4.309×10^{-6}	2.288×10^{-6}	5
Structural configuration	Hollow	2.543×10^{-6}	Solid	3.645×10^{-6}	1.101×10^{-6}	6

The calculated results show that the range of the flow-switching direction was the largest, reaching 4.602×10^{-6}, indicating that the flow-switching direction has the most significant influence on the maximum erosion rate. The opening area ranked second, with a range of 4.501×10^{-6}. The effects of the reduction angle, inlet flow capacity, and cutting particle size were relatively close, with ranges of 2.484×10^{-6}, 2.359×10^{-6}, and 2.288×10^{-6}, respectively. The structural form had the smallest range, 1.101×10^{-6}, suggesting that its influence on the maximum erosion rate is relatively weak within the operating conditions considered in this study.

Based on the range values, the relative influence of the factors on the maximum erosion rate can be ranked as follows: flow-switching direction > opening area > reduction angle > inlet flow capacity > cutting particle size > structural form.

5. Establishment of the Erosion Wear Prediction Model

5.1. Comparison of Prediction Algorithms and Model Selection

For erosion-rate predictions of the intelligent filling tool under flow-path switching conditions, several commonly used algorithms were first compared in this study. The results show that conventional multiple linear regression cannot describe the nonlinear relationship between the fluid kinetic energy and the collision angle, resulting in a low coefficient of determination (R^2) and evident underfitting. Although machine-learning algorithms such as the back-propagation neural network exhibit a strong nonlinear processing capability, they are highly prone to becoming trapped in local optima or overfitting under small-sample conditions, which reduces their prediction reliability; a similar limitation has been reported when response-surface and neural-network models were compared on small-sample erosion data.

Considering the drastic fluctuations in erosion-rate data over the order-of-magnitude range from 10^{-8} to 10^{-4} kg/(m^2·s), a stepwise quadratic response surface regression model based on a logarithmic transformation was ultimately selected in this study. By applying a logarithmic transformation, lg(E), this method effectively eliminates the interference of large order-of-magnitude variations on the regression accuracy, enabling balanced fidelity over the full range of erosion-rate magnitudes. Meanwhile, the stepwise regression algorithm is used to dynamically screen significant terms, which not only retains the interaction and quadratic terms that reveal physical coupling mechanisms, but also enhances the generalization capability of the model by eliminating redundant variables. To quantitatively evaluate the erosion risk under flow-path switching conditions, the model input and output variables were first defined as listed in Table 5.

Table 5. Definition of variables for the erosion-rate prediction model.

Symbol	Physical Meaning	Unit/Value Assignment
E	Predicted maximum erosion rate	kg/(m^2·s)
X_1	Reduction angle	°
X_2	Cutting particle size	mm
X_3	Inlet flow capacity	m^3/min
X_4	Flow-switching direction	0 for forward flow, 1 for reverse flow
X_5	Opening area	Number of holes in the physical structure
X_6	Structural form	0 for Model 1 (solid structure), 1 for Model 2 (hollow structure)

5.2. Model Construction Results and Algebraic Expression

Based on screening using the stepwise regression algorithm, the constructed model achieved a coefficient of determination of R^2 = 0.951 and an adjusted coefficient of determination of about 0.901. Together with the significance F-test, the root-mean-square error and the mean absolute error on the logarithmic scale, and the residual analysis, these metrics indicate that the model reasonably captured the relationship between the operating-condition factors and erosion damage within the present sample range. The final prediction equation for the maximum erosion rate of the intelligent filling tool and its mathematical expression were determined as follows:

$$\begin{aligned}\lg(E) = -17.1308 - 0.0307X_1 + 1.2707X_2 \\ +5.7023X_3 + 0.2735X_4 + 3.0422X_5 \\ -0.0095(X_1X_4) - 0.0098(X_1X_6) - 0.4316X_5^2\end{aligned} \quad (7)$$

The comparison between the predicted and observed values shows that, on the logarithmic scale, the sample points were generally distributed around the 1:1 ideal line, the residuals approximately followed a zero-mean random distribution, and no systematic deviation varying with the order of magnitude of the erosion rate was observed (Figure 11).

https://doi.org/10.3390/pr14152523

The composition of the significant terms shows that the model was dominated by several interaction terms, among which the interactions among the flow-switching direction, the opening area and the reduction angle were relatively prominent, indicating that the erosion rate is mainly governed by the coupling of the flow direction and the structural geometry, which is consistent with the factor ranking obtained from the range analysis. Limited by the sample size and the extrapolation capability of the model, this equation is recommended as a rapid reference for revealing the dominant erosion-controlling factors, for the preliminary optimization of operating parameters, and for assessing erosion trends, rather than as a high-precision predictor for extrapolation beyond the present conditions. Note on the use of Equation (7): the regression response is lg(E) (base-10 logarithm of the erosion rate in $kg \cdot m^{-2} \cdot s^{-1}$); accordingly, the predicted maximum erosion rate is recovered by the inverse (anti-logarithmic) transformation, i.e., by raising 10 to the power of the lg(E) value output by the right-hand side of Equation (7). All factor variables (X1–X6) are substituted at their native units or coded values as defined in Table 5 before the equation is evaluated. Equation (7) is further validated in Section 6, where its predictions are compared with the bench-test measurements of two specimens as worked examples.

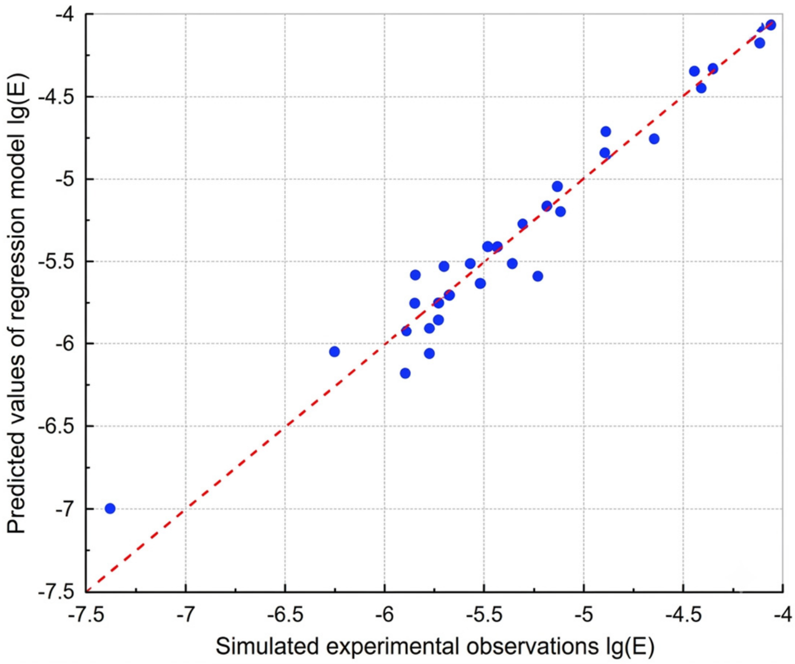

Figure 11. Prediction accuracy analysis plot of the stepwise regression model.

6. Experimental Validation

To validate the numerical erosion model established in this study, a series of jetting-erosion bench tests was performed under flow-path switching conditions, and the measured erosion rates were compared with the predicted values. Two erosion specimens, designated L80-1 and L80-2, were machined from API 5CT grade L80 carbon steel, a material widely used for downhole tubular goods in offshore sand-control completions. Both specimens were tested at a 90° reduction angle and a four-opening configuration at an inlet velocity of 1 m/s, corresponding to a volumetric flow rate of 28.3 m^3/h: specimen L80-1 under forward flow for 8 h, and specimen L80-2 under reverse flow for 6 h. The test conditions and the model-predicted erosion rates are listed in Table 6.

Table 6. Conditions and material specifications of erosion specimens used for CFD model validation.

Specimen	Material	Reduction Angle (°)	Flow Velocity (m/s)	Flow Rate (m^3/h)	Flow Direction	No. of Holes	Test Duration (h)	Predicted Erosion Rate, $kg \cdot m^{-2} \cdot s^{-1}$
L80-1	API 5CT L80 carbon steel	90	1	28.3	Forward	4	8	9.1×10^{-6}
L80-2	API 5CT L80 carbon steel	90	1	28.3	Reverse	4	6	4.4×10^{-5}

The erosion tests were performed on a circulating jetting-erosion test rig that reproduced the solid–liquid two-phase flow inside the filling tool. The rig mainly comprised a sand-laden-fluid tank with a stirring device, a centrifugal pump, a flow-regulating and metering unit, a test chamber housing the specimen together with the reduction section and the opening structure, and a return line. During operation, the stirrer kept the sand particles uniformly suspended, the pump drove the sand-laden fluid through the regulating valve into the test chamber, and the jet impinged on the specimen surface after passing through the reduction section and the openings before returning to the tank. The experimental medium, the sand-particle properties, the wall material and the structural dimensions were kept consistent with those adopted in the numerical model described in Sections 2 and 3, so that the test and the simulation were directly comparable. A photograph and a schematic diagram of the test apparatus are shown in Figure 12.

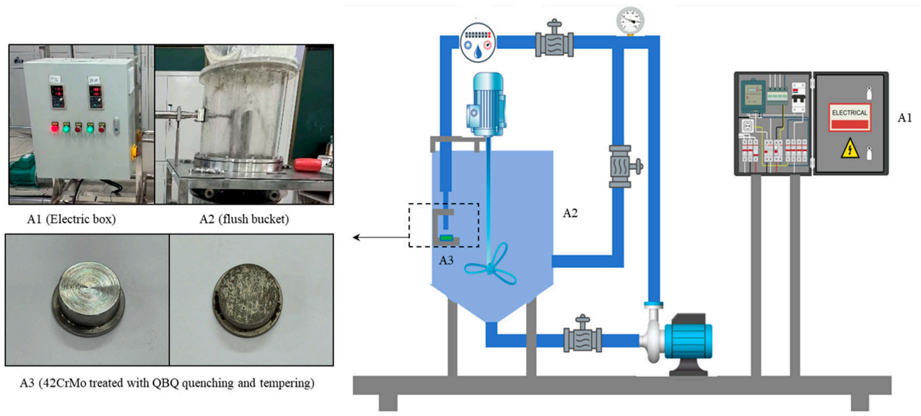

(**a**) (**b**)

Figure 12. Jetting-erosion test apparatus: photograph of the test rig (**a**) and schematic diagram (**b**).

Before testing, each specimen was cleaned, dried and weighed three times on an electronic balance with a resolution of 0.1 mg, and the mean value was taken as the initial mass. The specimen was then mounted in the test chamber at the position corresponding to the maximum-erosion region identified in the simulation. After running for the prescribed duration under the conditions listed in Table 6, the specimen was removed, ultrasonically cleaned, dried and re-weighed to obtain the final mass. The mass-flux erosion rate was then calculated from the recorded mass loss using Equation (8), and the measured values were compared with the model predictions to evaluate the accuracy of the numerical model.

The measured erosion rate of each specimen was calculated from Equation (8), using the specimen's recorded mass loss, the actual test duration, and the eroded surface area of 31.36 cm^2. The raw data and the resulting erosion rates are listed in Table 7. For specimen L80-1, Equation (8) yielded $E = 1.08 \times 10^{-5}$ $kg \cdot m^{-2} \cdot s^{-1}$; for specimen L80-2, it yielded $E = 5.47 \times 10^{-5}$ $kg \cdot m^{-2} \cdot s^{-1}$. At the common inlet velocity of 1 m/s, the reverse-flow specimen therefore eroded 5.07 times faster than the forward-flow specimen, closely matching the 4.8-fold difference returned by Equation (7) and confirming the simulation finding that reverse flow is the more damaging operating condition. The predicted and measured erosion rates are compared in Table 8.

$$E = \frac{\Delta m}{A \cdot t} \tag{8}$$

where E is the mass-flux erosion rate in kg·m^{-2}·s^{-1}, m is the specimen mass loss in kg, A is the eroded surface area of the specimen coupon in m^2, and t is the test duration in s. The eroded surface area A corresponds to the face of the specimen coupon directly exposed to the jetting flow. The calculated erosion rates of the two validation specimens are listed in Table 6.

Table 7. Raw experimental data and measured erosion rates of the validation specimens.

No.	Specimen ID	Reduction Angle (°)	Flow Velocity (m/s)	Converted Flow Rate (m^3/h)	Mass Before Erosion (g)	Mass After Erosion (g)	Test Duration (h)	Erosion Rate kg·m^{-2}·s^{-1}
1	L80-1	90	1	28.3	24.0367	23.0615	8	1.08×10^{-5}
2	L80-2	90	1	28.3	24.1232	20.4148	6	5.47×10^{-5}

Table 8. Accuracy validation of the erosion-prediction equation: measured versus predicted erosion rates and relative errors.

No.	Specimen ID	Reduction Angle (°)	Flow Velocity (m/s)	Measured Erosion Rate kg·m^{-2}·s^{-1}	Predicted Value, Equation (7) kg·m^{-2}·s^{-1}	Relative Error (%)
1	L80-1	90	1	1.08×10^{-5}	9.09×10^{-6}	−15.8
2	L80-2	90	1	5.47×10^{-5}	4.37×10^{-5}	−20.1

Beyond the quantitative comparison, the eroded surface morphologies in Figure 13 provide independent, qualitative support for the simulated erosion pattern. On the forward-flow specimen (L80-1), both sampled locations exhibited a single, well-bounded crater with a smoothly graded, concentric depth profile that deepened toward one dominant center rather than spreading across the surface; this compact, single-hot-spot morphology closely mirrors the sharply localized, X-shaped high-erosion-rate zone predicted by the simulation at the reduction shoulder under forward flow, as shown in Figure 6, confirming that particle impingement under forward flow remains concentrated at one persistent site. The reverse-flow specimen (L80-2), in contrast, displayed a more irregular and spatially extended damage pattern: an elongated band of moderate-to-high wear surrounded two to three discrete pits rather than collapsing into a single crater. This multi-lobed distribution is consistent with the broader, less symmetric erosion-rate contour that the simulation predicted for reverse flow, where recirculation near the opening structure redirects sand particles toward more than one impingement site instead of a single concentrated point. The qualitative agreement between the photographed/profiled damage patterns and the simulated erosion contours, together with the quantitative agreement reported in Table 8, jointly support the validity of the numerical erosion model.

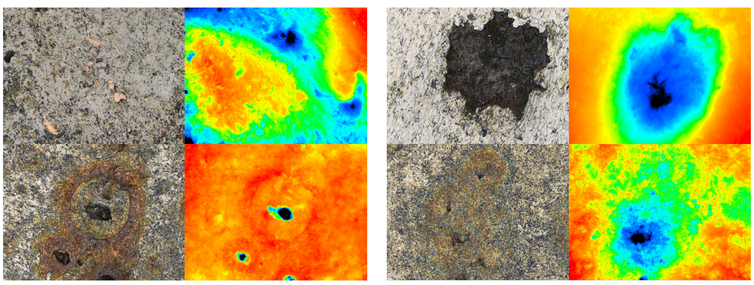

Figure 13. Eroded surface morphologies of the validation specimens after testing.

As shown in Table 8, the predicted erosion rates from Equation (7) agreed closely with the measured values: the relative errors were −15.8% for specimen L80-1 and −20.1% for specimen L80-2. Both deviations fell within the scatter that is routinely observed in sand-erosion bench testing, and their consistent sign indicates a small, systematic conservative bias rather than a direction-dependent error. The predicted reverse-to-forward erosion ratio of 4.8 also agrees well with the measured ratio of 5.1, confirming that Equation (7) captures not only the direction, but also the approximate magnitude of the flow-switching effect. Taken together, these two validation points support the use of Equation (7), both for ranking the dominant erosion-controlling factors and for quantitatively estimating the erosion rate under field-relevant operating conditions. As with any response-surface model calibrated on a limited design matrix, predictions outside the sampled parameter range should be treated with appropriate caution.

7. Conclusions

This study focused on an intelligent filling tool under flow-path switching conditions. Numerical simulations were conducted to analyze the flow characteristics of a sand-laden fluid inside the tool, the particle motion behavior, and the wall erosion characteristics. In addition, a range analysis and erosion-rate prediction model development were performed based on the results of orthogonal experiments. The main conclusions are as follows:

(1) Under flow-path switching conditions, the internal flow field of the intelligent filling tool exhibited strong non-uniformity. When the sand-laden fluid passed through the switching flow path, the particles were affected by the reduction section and abrupt changes in the flow direction. Owing to their inertia, the particles could not promptly follow the deflected streamlines and were therefore prone to concentrated impacts at the reduction shoulder, opening edges, and flow-turning regions. The presence of local high-velocity jets and secondary recirculation zones further intensified the cutting action of sand particles on the wall surface.

(2) The range analysis indicates that, within the operating conditions considered in this study, the flow-switching direction is the dominant factor affecting the maximum erosion rate of the intelligent filling tool. The maximum erosion rate increases significantly under reverse-flow conditions. The influence of the opening area on the erosion rate is second only to that of the flow-switching direction, and increasing the opening area is beneficial for reducing the local erosion intensity. The reduction angle, inlet flow capacity, and cutting particle size also exert certain effects on the erosion rate, whereas the influence of the structural form is relatively weak. Based on the range analysis results, the preferred parameter combination for reducing the erosion rate is forward flow, a four-opening configuration, a 20° reduction angle, a relatively low inlet flow capacity, a 5 mm cutting particle size, and a hollow structure.

(3) The effect of the cutting particle size on the erosion rate exhibited nonlinear characteristics. Within the range investigated in this study, particles with a diameter of approximately 3 mm presented the highest erosion risk. These particles possessed a sufficient impact mass while maintaining a strong flow-following capability, allowing them to impinge accurately on erosion-sensitive regions. In contrast, excessively large or small particles contributed slightly less to the maximum erosion rate because of excessive inertia or overly strong flow-following behavior, respectively.

(4) Considering the cross-order-of-magnitude distribution and the strong nonlinearity of erosion-rate data, a stepwise quadratic response surface regression model based on a logarithmic transformation was selected and established in this study. The results demonstrate that the conventional linear regression model provided an insufficient goodness of fit, with R^2 = 0.64, whereas the proposed method increased the coefficient

of determination to $R^2 = 0.951$ (adjusted coefficient of determination of about 0.901) through a logarithmic transformation and significant-feature screening. This model not only retains the interaction and quadratic terms that reveal physical coupling mechanisms, but it also provides a concise algebraic expression; within the present sample range, it can reasonably estimate the erosion damage rate under different combinations of operating conditions and is suitable for revealing dominant factors and for preliminary parameter optimization.

(5) Forward-flow operation, a 20° gradual-reduction geometry and a multi-opening configuration are recommended as the preferred design and operating choices for intelligent filling tools, as this combination consistently produced the lowest erosion rates across the orthogonal simulation matrix. The prediction model regressed lg(E) rather than E directly, and the erosion rate was recovered by taking the anti-logarithm of the predicted lg(E) value. Within the sampled parameter range, the model reproduced the bench-test erosion rates of the two validation specimens to within 15.8% (forward flow) and 20.1% (reverse flow), with the predicted and measured reverse-to-forward erosion ratios in close agreement (4.8 versus 5.1); this level of accuracy supports the use of the model as a practical basis for field operating-parameter optimization and a preliminary service-life assessment of the tool.

(6) For engineering applications, the factor ranking obtained from the orthogonal analysis together with the erosion-prediction model established in this study can be used to screen structural schemes and operating parameters for erosion risk before field deployment. To reduce the maximum erosion rate, a forward-flow operation, a four-opening configuration, a 20° reduction angle and a relatively low inlet flow capacity are recommended, while the reduction shoulder, the opening edges and the flow-turning regions—identified as the erosion hot spots—should be locally strengthened or protected by wear-resistant treatment.

Finally, it should also be noted that the present conclusions are subject to certain limitations. The validation is based on a limited number of bench tests, and the particle phase is described by the discrete phase model under a relatively low sand concentration, so the applicability of the model to dense-phase and high-concentration flows still requires further verification. In addition, the wall hardness was treated as a fixed parameter without considering corrosion–erosion coupling, and, as a response-surface model calibrated on a limited design matrix, the prediction equation should be applied with caution outside the sampled parameter range; its extension to larger-scale structures requires a dedicated dimensionless framework. These aspects will be addressed in future work.

Author Contributions: Conceptualization, K.Z.; Methodology, B.W.; Resources, J.L.; Data Curation, Y.Z.; Writing—Original Draft, Y.Z.; Writing—Review and Editing, C.L.; Visualization, M.Z. All authors have read and agreed to the published version of the manuscript.

Funding: This work was supported by China National Offshore Oil Corporation (China) (KJZH-2024-1303) and National Natural Science Foundation of China (Grant No. 52274018).

Data Availability Statement: The original contributions presented in this study are included in the article. Further inquiries can be directed to the corresponding author.

Conflicts of Interest: Authors Kai Zuo, Binggang Wang, Yunchi Zhang, Chuangang Liu and Jingchao Liu were employed by the CNOOC Energy Technology & Services Limited Key Laboratory for Offshore Completion and the CNOOC EnerTech-Drilling & Production Co. The authors declare that the research was conducted in the absence of any commercial or financial relationships that could be construed as a potential conflict of interest. The authors declare that this study received funding from the China National Offshore Oil Corporation (China). The funder was not involved in the study

design; the collection, analysis, or interpretation of data; the writing of this article; or the decision to submit it for publication.

References

1. Finnie, I. Erosion of Surfaces by Solid Particles. *Wear* **1960**, *3*, 87–103. [CrossRef]
2. Levy, A.V. The Platelet Mechanism of Erosion of Ductile Metals. *Wear* **1986**, *108*, 1–21. [CrossRef]
3. Bitter, J.G.A. A Study of Erosion Phenomena Part I. *Wear* **1963**, *6*, 5–21. [CrossRef]
4. Bitter, J.G.A. A Study of Erosion Phenomena: Part II. *Wear* **1963**, *6*, 169–190. [CrossRef]
5. Neilson, J.H.; Gilchrist, A. Erosion by a Stream of Solid Particles. *Wear* **1968**, *11*, 111–122. [CrossRef]
6. Tilly, G.P. A Two Stage Mechanism of Ductile Erosion. *Wear* **1973**, *23*, 87–96. [CrossRef]
7. Morsi, S.A.; Alexander, A.J. An Investigation of Particle Trajectories in Two-Phase Flow Systems. *J. Fluid Mech.* **1972**, *55*, 193–208. [CrossRef]
8. Crowe, C.T.; Sharma, M.P.; Stock, D.E. The Particle-Source-In Cell (PSI-CELL) Model for Gas-Droplet Flows. *J. Fluids Eng.* **1977**, *99*, 325–332. [CrossRef]
9. Gosman, A.D.; Loannides, E. Aspects of Computer Simulation of Liquid-Fueled Combustors. *J. Energy* **1983**, *7*, 482–490. [CrossRef]
10. Shih, T.-H.; Liou, W.W.; Shabbir, A.; Yang, Z.; Zhu, J. A New k-ϵ Eddy Viscosity Model for High Reynolds Number Turbulent Flows. *Comput. Fluids* **1995**, *24*, 227–238. [CrossRef]
11. Pereira, G.C.; de Souza, F.J.; de Moro Martins, D.A. Numerical Prediction of the Erosion Due to Particles in Elbows. *Powder Technol.* **2014**, *261*, 105–117. [CrossRef]
12. Mansouri, A.; Arabnejad, H.; Karimi, S.; Shirazi, S.A.; McLaury, B.S. Improved CFD Modeling and Validation of Erosion Damage Due to Fine Sand Particles. *Wear* **2015**, *338–339*, 339–350. [CrossRef]
13. Parsi, M.; Al-Sarkhi, A.; Kara, M.; Sharma, P.; McLaury, B.S.; Shirazi, S.A. A New Dimensionless Number for Solid Particle Erosion in Natural Gas Elbows. *Wear* **2017**, *390–391*, 80–83. [CrossRef]
14. Arabnejad, H.; Mansouri, A.; Shirazi, S.A.; McLaury, B.S. Development of Mechanistic Erosion Equation for Solid Particles. *Wear* **2015**, *332–333*, 1044–1050. [CrossRef]
15. Zhang, Y.; Reuterfors, E.P.; McLaury, B.S.; Shirazi, S.A.; Rybicki, E.F. Comparison of Computed and Measured Particle Velocities and Erosion in Water and Air Flows. *Wear* **2007**, *263*, 330–338. [CrossRef]
16. Oka, Y.I.; Okamura, K.; Yoshida, T. Practical Estimation of Erosion Damage Caused by Solid Particle Impact: Part 1: Effects of Impact Parameters on a Predictive Equation. *Wear* **2005**, *259*, 95–101. [CrossRef]
17. Oka, Y.I.; Yoshida, T. Practical Estimation of Erosion Damage Caused by Solid Particle Impact: Part 2: Mechanical Properties of Materials Directly Associated with Erosion Damage. *Wear* **2005**, *259*, 102–109. [CrossRef]
18. Forder, A.; Thew, M.; Harrison, D. A Numerical Investigation of Solid Particle Erosion Experienced within Oilfield Control Valves. *Wear* **1998**, *216*, 184–193. [CrossRef]
19. Solnordal, C.B.; Wong, C.Y.; Boulanger, J. An Experimental and Numerical Analysis of Erosion Caused by Sand Pneumatically Conveyed through a Standard Pipe Elbow. *Wear* **2015**, *336–337*, 43–57. [CrossRef]
20. Zamani, M.; Seddighi, S.; Nazif, H.R. Erosion of Natural Gas Elbows Due to Rotating Particles in Turbulent Gas-Solid Flow. *J. Nat. Gas. Sci. Eng.* **2017**, *40*, 91–113. [CrossRef]
21. Nøkleberg, L.; Søntvedt, T. Erosion of Oil&gas Industry Choke Valves Using Computational Fluid Dynamics and Experiment. *Int. J. Heat Fluid Flow* **1998**, *19*, 636–643. [CrossRef]
22. Bilal, F.S.; Sedrez, T.A.; Shirazi, S.A. Experimental and CFD Investigations of 45 and 90 Degrees Bends and Various Elbow Curvature Radii Effects on Solid Particle Erosion. *Wear* **2021**, *476*, 203646. [CrossRef]
23. Vieira, R.E.; Mansouri, A.; McLaury, B.S.; Shirazi, S.A. Experimental and Computational Study of Erosion in Elbows Due to Sand Particles in Air Flow. *Powder Technol.* **2016**, *288*, 339–353. [CrossRef]
24. Zhang, J.X.; Bai, Y.Q.; Kang, J.; Wu, X. Failure Analysis and Erosion Prediction of Tee Junction in Fracturing Operation. *J. Loss Prev. Process Ind.* **2017**, *46*, 94–107. [CrossRef]
25. Duarte, C.A.R.; de Souza, F.J. Innovative Pipe Wall Design to Mitigate Elbow Erosion: A CFD Analysis. *Wear* **2017**, *380–381*, 176–190. [CrossRef]
26. Mazur, Z.; Campos-Amezcua, R.; Urquiza-Beltrán, G.; García-Gutiérrez, A. Numerical 3D Simulation of the Erosion Due to Solid Particle Impact in the Main Stop Valve of a Steam Turbine. *Appl. Therm. Eng.* **2004**, *24*, 1877–1891. [CrossRef]
27. Chen, X.; McLaury, B.S.; Shirazi, S.A. Numerical and Experimental Investigation of the Relative Erosion Severity between Plugged Tees and Elbows in Dilute Gas/Solid Two-Phase Flow. *Wear* **2006**, *261*, 715–729. [CrossRef]
28. Zhu, H.; Qi, Y. Numerical Investigation of Flow Erosion of Sand-Laden Oil Flow in a U-Bend. *Process Saf. Environ. Prot.* **2019**, *131*, 16–27. [CrossRef]
29. Deng, F.; Yin, B.; Xiao, Y.; Li, G.; Yan, C. Research on Erosion Wear of Slotted Screen Based on High Production Gas Field. *Processes* **2022**, *10*, 1640. [CrossRef]

30. Abduljabbar, A.; Mohyaldinn, M.E.; Younis, O.; Alghurabi, A.; Alakbari, F.S. Erosion of Sand Screens by Solid Particles: A Review of Experimental Investigations. *J. Petrol. Explor. Prod. Technol.* **2022**, *12*, 2329–2345. [CrossRef]
31. Abduljabbar, A.; Mohyaldinn, M.; Younis, O.; Alghurabi, A. A Numerical CFD Investigation of Sand Screen Erosion in Gas Wells: Effect of Fine Content and Particle Size Distribution. *J. Nat. Gas. Sci. Eng.* **2021**, *95*, 104228. [CrossRef]
32. Ma, C.; Deng, J.; Feng, Y.; Li, S.; Li, X. The Influence of Structural Parameters on the Plugging of Prepacked Gravel Screens. *Rock. Mech. Rock. Eng.* **2021**, *54*, 6135–6153. [CrossRef]
33. Zhang, R.; Hao, S.; Zhang, C.; Meng, W.; Zhang, G.; Liu, Z.; Gao, D.; Tang, Y. Analysis and Simulation of Erosion of Sand Control Screens in Deep Water Gas Well and Its Practical Application. *J. Pet. Sci. Eng.* **2020**, *189*, 106997. [CrossRef]
34. Box, G.E.P.; Cox, D.R. An Analysis of Transformations. *J. R. Stat. Soc. Ser. B Stat. Methodol.* **1964**, *26*, 211–243. [CrossRef]
35. Montgomery, D.C. *Design and Analysis of Experiments*, 9th ed.; Wiley: Hoboken, NJ, USA, 2022.
36. Box, G.E.P.; Wilson, K.B. On the Experimental Attainment of Optimum Conditions. *J. R. Stat. Soc. Ser. B Stat. Methodol.* **1951**, *13*, 1–38. [CrossRef]
37. Ross, P.J. *Taguchi Techniques for Quality Engineering: Loss Function, Orthogonal Experiments, Parameter and Tolerance Design*; McGraw-Hill: New York, NY, USA, 1988.
38. Bagheri, M.; Ranjbar Malidarreh, N.; Ghaseminejad, V.; Asgari, A. Seismic Resilience Assessment of RC Superstructures on Long–Short Combined Piled Raft Foundations: 3D SSI Modeling with Pounding Effects. *Structures* **2025**, *81*, 110176. [CrossRef]